Available online at www.sciencedirect.com
ScienceDirect
Journal of Sound and Vibration 307 (2007) 2–19
JOURNAL OF SOUND AND VIBRATION
www.elsevier.com/locate/jsvi

Repetitive impact response of a beam structure subjected to harmonic base excitation

Elizabeth K. Ervin[a], J.A. Wickert[b,*]

[a]Department of Civil Engineering, University of Mississippi, University, MS 38677, USA
[b]Department of Mechanical Engineering, Iowa State University, Ames, Iowa 50011, USA

Received 22 October 2005; received in revised form 28 July 2006; accepted 7 June 2007

Abstract

This paper investigates the forced response dynamics of a clamped–clamped beam to which a rigid body is attached, and in the presence of periodic or non-periodic impacts between the body and a comparatively compliant base structure. The assembly is subjected to base excitation at specified frequency and acceleration, and the potentially complex responses that occur are examined analytically. The two sets of natural frequencies and vibration modes of the beam-rigid body structure (in its in-contact state, and in its not-in-contact state), are used to treat the forced response problem through a series of algebraic mappings among those states. A modal analysis based on extended operators for the (continuous) beam and (discrete) rigid body establishes a piecewise linear state-to-state mapping for transition between the in-contact and not-in-contact conditions. The contact force, impulse, and displacement each exhibit complex response characteristics as a function of the excitation frequency. Periodic responses occurring at the excitation frequency, period-doubling bifurcations, grazing impacts, sub-harmonic regions, fractional harmonic resonances, and apparently chaotic responses each occur at various combinations of damping, excitation frequency, and contact stiffness. The results of parameter studies in structural asymmetry and the eccentricity of the contact point's location are discussed.
© 2007 Elsevier Ltd. All rights reserved.

1. Introduction

Impact in structures can occur as a result of clearances and manufacturing tolerances, or through intermittent contact between rotating or translating machine elements. Excessive clearance between an engine's piston and the cylinder wall, for instance, enables the piston to move laterally and impact the cylinder with each stroke [1]. Turbomachinery blades are likewise sensitive to imbalance, and their vibration leads to high cycle fatigue problems which can be addressed, in part, through self-tuning impact dampers [2].

Aside from machine dynamics, nuclear power plants are one class of structures for which impact-driven vibration is of concern. Steam generator tubes and reactor control rods, for instance, can contact their supporting structures. The resulting impacts and vibration not only can damage those components, but they can introduce contaminants into the reactor's fluids systems. In pressurized water reactors, the primary

*Corresponding author.
E-mail address: wickert@iastate.edu (J.A. Wickert).

0022-460X/$ - see front matter © 2007 Elsevier Ltd. All rights reserved.
doi:10.1016/j.jsv.2007.06.038

coolant for the reactor compartment flows through thousands of meters of tubing within the steam generators. Support plates are used to control and minimize, but not necessarily eliminate, lateral motion of the thousands of tubes present in each generator. Impact of any particular tube against its support structure increases the risk of fracture and leakage could contaminate the secondary fluid loop [3].

Reactor fuel rods are another application in which a slender beam-like structure is subjected to impact. In that case, the rod's designed end conditions vary from being "seated" (where the rod rests in a fitted cup) to "floating" (where the reactor's cap produces elastic hold-down forces). Spacer grids support the overall fuel assembly structure and prevent the rods from impacting one another while still enabling the primary coolant to flow freely [4]. Impact can cause undesirable fretting and wear of such sensitive components.

Related literature on the subject of impact dynamics includes studies of discrete and continuous systems that are subjected to impact under various circumstances. Shaw and Holmes [5] examined a single-degree-of-freedom system comprising a concentrated mass that can impact a spring and that is otherwise free between collisions. This piecewise linear system's response spectrum exhibited periodic responses, period-doubling bifurcations, and chaotic response regimes. Fourier [6], continuation [7], harmonic balance [8], and finite element [9–11] methods have each been applied to study specific impact oscillator systems. Maezawa et al. [6] represented the steady-state response of an impacting single-degree-of-freedom oscillator through a Fourier series. In addition to the features reported in Ref. [5], superharmonics developed at higher values of the contact stiffness. Xu et al. [12] applied the incremental harmonic balance method to analyze a nonlinear single-degree-of-freedom system that exhibited multiple bifurcations and regions of chaos. While examining structural dampers for a vibrating beam, Bonsel et al. [13] experimentally verified the occurrence of multiple harmonics and subharmonics in the structure's repetitive impact frequency response. Fang and Wickert [14] examined the vibration of a cantilever beam subjected to repetitive tip impact, and found a recurring pattern of resonance, bifurcation, and non-periodic motions.

2. Vibration model

Fig. 1 illustrates the schematic of a rigid body having mass m and mass moment of inertia J that is supported by two Euler–Bernoulli beams having clamped end conditions. Each beam segment $i = 1$ or 2 is rectangular in cross-section with areas A_i as the product of depth b_i and height h_i, and the second moments of area are denoted $I_i = b_i h_i^3/12$. Beam portions "1" and "2" likewise have flexural rigidities E_1I_1 and E_2I_2, volumetric densities ρ_1 and ρ_2, and lengths L_1 and L_2. Illustrative numerical values for the model parameters

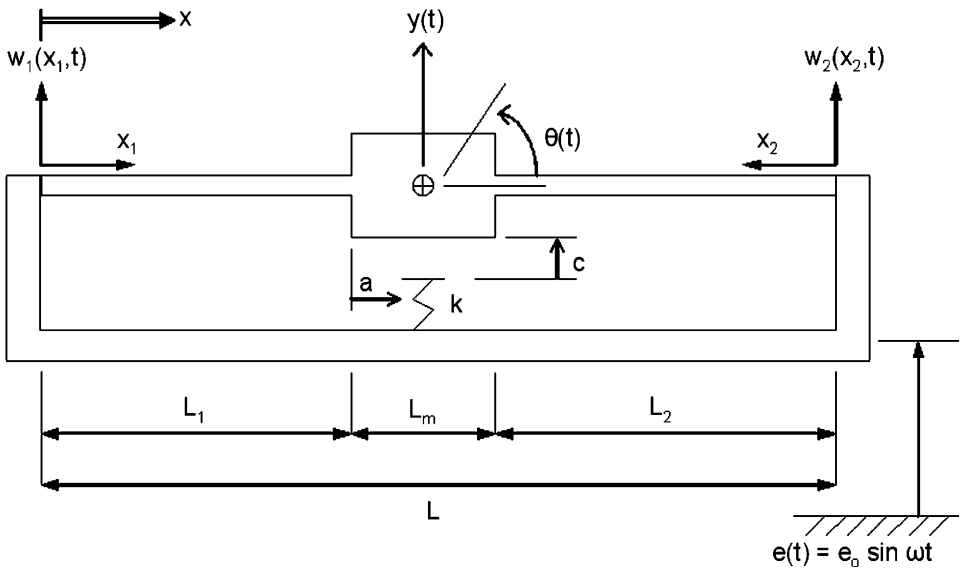

Fig. 1. Model of a rigid body, supported by two elastic beams, that is subjected to base excitation and impact.

Table 1
Nominal parameters used in the case studies

System	
Length, L (m)	1.52×10^{-1}
Contact location, a (m)	1.27×10^{-2}
Clearance, c (m)	0
Beam 1	
Modulus, E_1 (GPa)	69
Density, ρ_1 (kg/m^3)	2.69×10^{3}
Length, L_1 (m)	6.35×10^{-2}
Height, h_1 (m)	3.02×10^{-3}
Width, b_1 (m)	2.54×10^{-2}
Rigid body	
Length, L_m (m)	2.54×10^{-2}
Mass, m (kg)	3.30×10^{-2}
Rotational inertia, J (kg/m^2)	7.17×10^{-9}
Beam 2	
Modulus, E_2 (GPa)	69
Density, ρ_2 (kg/m^3)	2.69×10^{3}
Length, L_2 (m)	6.35×10^{-2}
Height, h_2 (m)	3.02×10^{-3}
Width, b_2 (m)	2.54×10^{-2}

used in the later case studies are listed in Table 1. The displacements of the beam portions on either side of the rigid body are denoted by $w_1(x_1, t)$ and $w_2(x_2, t)$ where the local coordinates are $x_1 = x$ and $x_2 = L - x$.

The motion of the rigid body couples with the beams through its translational y and rotational θ degrees of freedom, where y denotes the centroidal displacement. Contact between the rigid body and the supporting base structure occurs on the rigid body at distance a along its full length L_m, as indicated in the diagram. The symmetry (or asymmetry) of the structure about the rigid body's centroid, the clearance or stand-off gap distance c, and the contact stiffness k can each be varied in simulation. Motion of the combined rigid body and two-beam system is viewed as switching sequentially between two states $S^{(j)}$ within which vibration is linear: state $j = 0$ refers to the configuration in which the rigid body does not contact the spring, and state $j = 1$ refers to the case in which the body does contact the spring.

The configuration of the system in either state is given by:

$$\underline{v}^{(j)} = [w_1 \;\; w_2 \;\; y \;\; \theta]^{\mathrm{T}}, \tag{1}$$

where the first two elements of the vector are functions of position and time, and the second two elements are functions of time only. Geometric compatibility between the rigid body and beams requires

$$\begin{aligned} y(t) &= w_1(L_1, t) + (L_m/2) w_{1,x}(L_1, t) \\ &= w_2(L_2, t) + (L_m/2) w_{2,x}(L_2, t), \end{aligned} \tag{2}$$

$$\theta(t) = w_{1,x}(L_1, t) = -w_{2,x}(L_2, t), \tag{3}$$

where the comma-subscript notation implies partial differentiation. For brevity here and in what follows, the term "x" subscript denotes differentiation with respect to x_1 for terms involving w_1, and with respect to x_2 for terms involving w_2.

The compatibility conditions among the beam segments are

$$w_2(L_2, t) = w_1(L_1, t) + L_m w_{1,x}(L_1, t), \tag{4}$$

$$w_{1,x}(L_1, t) = -w_{2,x}(L_2, t). \tag{5}$$

The remaining boundary conditions for the beam segments represent the clamped supports and prescribed base excitation $e(t)$: $w_1(0,t) = e(t)$, $w_{1,x}(0,t) = 0$, $w_2(0,t) = e(t)$, and $w_{2,x}(0,t) = 0$. The equations of motion for the beam portions are

$$\rho_1 A_1 w_{1,tt} + E_1 I_1 w_{1,xxxx} = 0, \tag{6}$$

$$\rho_2 A_2 w_{2,tt} + E_2 I_2 w_{2,xxxx} = 0. \tag{7}$$

In $S^{(0)}$, the equations of motion for the rigid body are

$$m y_{,tt} = E_1 I_1 w_{1,xxx}(L_1,t) + E_2 I_2 w_{2,xxx}(L_2,t), \tag{8}$$

$$\begin{aligned} J\theta_{,tt} = & -E_1 I_1 w_{1,xx}(L_1,t) + E_2 I_2 w_{2,xx}(L_2,t) \\ & - \frac{Lm}{2} E_1 I_1 w_{1,xxx}(L_1,t) + \frac{Lm}{2} E_2 I_2 w_{2,xxx}(L_2,t). \end{aligned} \tag{9}$$

The latter expression incorporates the influence of the beams' end shears, which were not considered in Ref. [15]. In $S^{(1)}$, terms representing the contact spring's restoring force and moment about the body's centroid are appended to Eqs. (8) and (9).

The equations of motion for the rigid body and the two beam segments are written in a structured manner in terms of extended operators. The advantage of such an approach is that modal analysis can be employed in a standard fashion, notwithstanding the presence of eigenvalues in the boundary condition expressions. The coupled Eqs. (6)–(9) are written in terms of the vector $\underline{v}$

$$\underline{M}\,\underline{v}_{,tt} + \underline{K}\,\underline{v} = 0, \tag{10}$$

in either state, where the inertia operator $\underline{M}$ is

$$\underline{M}^{(j)}\,\underline{v} = \begin{bmatrix} \rho_1 A_1 w_1(x,t) \\ \rho_2 A_2 w_2(x,t) \\ m y(t) \\ J\theta(t) \end{bmatrix}. \tag{11}$$

The stiffness operator in $S^{(0)}$ is

$$\underline{K}^{(0)}\,\underline{v} = \begin{bmatrix} E_1 I_1 w_{1,xxxx}(x,t) \\ E_2 I_2 w_{2,xxxx}(x,t) \\ -E_1 I_1 w_{1,xxx}(L_1,t) - E_2 I_2 w_{2,xxx}(L_2,t) \\ E_1 I_1 w_{1,xx}(L_1,t) - E_2 I_2 w_{2,xx}(L_2,t) \\ \quad + E_1 I_1 \dfrac{L_m}{2} w_{1,xxx}(L_1,t) - E_2 I_2 \dfrac{L_m}{2} w_{2,xxx}(L_2,t) \end{bmatrix} \tag{12}$$

and in $S^{(1)}$ it is given by

$$\underline{K}^{(1)}\,\underline{v} = \underline{K}^{(0)}\,\underline{v} + \begin{bmatrix} 0 \\ 0 \\ k y(t) - k\theta(t)\left(\dfrac{L_m}{2} + a\right) \\ k\left(a - \dfrac{L_m}{2}\right) y(t) - ka\left(a - \dfrac{L_m}{2}\right)\theta(t) \end{bmatrix}. \tag{13}$$

The impetus for the extended operator formulation is that the inertia and stiffness operators for each state are self-adjoint. With respect to the inner product with the arbitrary vector $\underline{r} = [r_1\ r_2\ r_3\ r_4]^{\mathrm{T}}$,

for instance

$$\begin{aligned}\langle \underline{K}^{(0)}\,\underline{v},\underline{r}\rangle = &\int_0^{L_1} E_1 I_1 w_{1,xxxx} r_1\,\mathrm{d}x_1 + \int_0^{L_2} E_2 I_2 w_{2,xxxx} r_2\,\mathrm{d}x_2\\ &+ [-E_1 I_1 w_{1,xxx}|_{L_1} - E_2 I_2 w_{2,xxx}|_{L_2}] r_3\\ &+ [E_1 I_1 w_{1,xx}|_{L_1} - E_2 I_2 w_{2,xx}|_{L_2}\\ &+ E_1 I_1 \frac{L_m}{2} w_{1,xxx}|_{L_1} - E_2 I_2 \frac{L_m}{2} w_{2,xxx}|_{L_2}] r_4\end{aligned} \tag{14}$$

is identical to $\langle \underline{K}^{(0)}\,\underline{r},\underline{v}\rangle$.

In Fig. 1, the beam is subjected to base vibration $e(t) = e_0 \sin(\omega t)$. With the superposition $\underline{v} = \underline{u} + [e(t)\ e(t)\ 0\ 0]^{\mathrm{T}}$, the boundary conditions on w_1 and w_2 become homogeneous. The equation of motion then becomes

$$\underline{M}\,\underline{u}_{,tt} + \underline{K}\,\underline{u} = \underline{f} \tag{15}$$

with the body force vector

$$\underline{f} = [-\rho_1 A_1 e_{,tt} \quad -\rho_2 A_2 e_{,tt} \quad -m e_{,tt} \quad 0]^{\mathrm{T}}. \tag{16}$$

3. Free vibration in $S^{(0)}$ and $S^{(1)}$

Synchronous solutions for free vibration within either state $S^{(j)}$ are sought such that $\underline{u}^{(j)} = \underline{\phi}^{(j)} \sin(\omega t)$. The mode shapes $\underline{\phi}^{(j)}$ are given by

$$\underline{\phi}^{(j)} = [W_1(x) \quad W_2(x) \quad Y \quad \Theta]^{\mathrm{T}}, \tag{17}$$

where Y and Θ are constant amplitudes. Since $\underline{M}$ and $\underline{K}$ are self-adjoint, these mode shapes are orthogonal with respect to the aforementioned operators and inner product. With the subscripts p and q denoting two different modes in $S^{(j)}$, the orthonormality relationships between $\phi_p^{(j)}$ and $\phi_q^{(j)}$ are $\langle \underline{M}\,\underline{\phi}_p^{(j)}, \underline{\phi}_q^{(j)}\rangle = \delta_{pq}$ and $\langle \underline{K}\,\underline{\phi}_p^{(j)}, \underline{\phi}_q^{(j)}\rangle = \omega_p^{(j)2}\delta_{qp}$ (no sum).

The modal deflection over each beam segment i is written as a superpositions of terms $A\sin(\gamma x) + B\cos(\gamma x) + C\sinh(\gamma x) + D\cosh(\gamma x)$, where $\gamma^2 = E_i I_i/(\rho_i A_i)$, in either $S^{(j)}$. Coordinates Y and Θ are also expressed in terms of these coefficients through Eqs. (2) and (3). Together, Eqs. (4)–(5), Eqs. (8)–(9), and the remaining boundary conditions provide the constraints necessary to determine the beams' displacement coefficients. The resulting characteristic equation for each state j is an eigenvalue problem for the system's natural frequencies ω_i and mode shapes.

Figs. 2 and 3 depict mode shapes at the parameter values listed in Table 1, for which the structure is symmetric about the rigid body's centroid. Here the (scalar) $\phi_i^{(j)}$ denotes the modal displacement field of the rigid body and two beams over $x \in (0, L)$. The spatial coordinates are normalized by the total length L so that $x^* = x/L \in (0, 1)$. For each symmetric mode, the rigid body has zero slope, and the beam segments are subjected effectively to clamped boundary conditions. In $S^{(1)}$, the contact spring further constrains motion of the body. The reduction in modal amplitude at the centroid is directly related to the magnitude of k and the contact force. Force terms are non-dimensionalized with respect to the structure's static stiffness k_b to a force applied at, and displacement measured at, the body's centroid. At low values, the contact stiffness has little effect on the $S^{(1)}$ mode shapes. Fig. 3 depicts the first four mode shapes for the system while in contact with the spring, for $k^* = k/k_b = 10^5$. Here the spring contacts the rigid body's centroidal line, which is a nodal point for the anti-symmetric modes. The first anti-symmetric mode in Fig. 3 has the lowest natural frequency, which is the case for $k^* > 3.3 \times 10^4$. The spring strongly influences the first symmetric mode and reduces the rigid body's deflection by 12.1% relative to the corresponding mode in $S^{(0)}$.

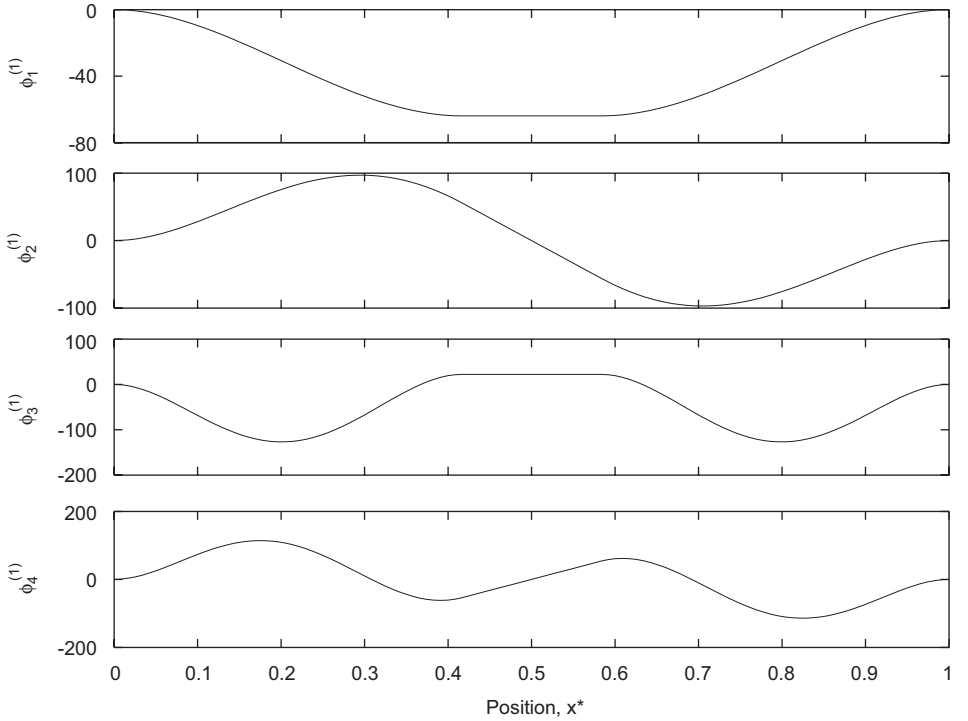

Fig. 2. First four normalized mode shapes in $S^{(0)}$; $\omega_i^* = 1$, 3.46, 8.74, and 11.11. Parameters are as listed in Table 1.

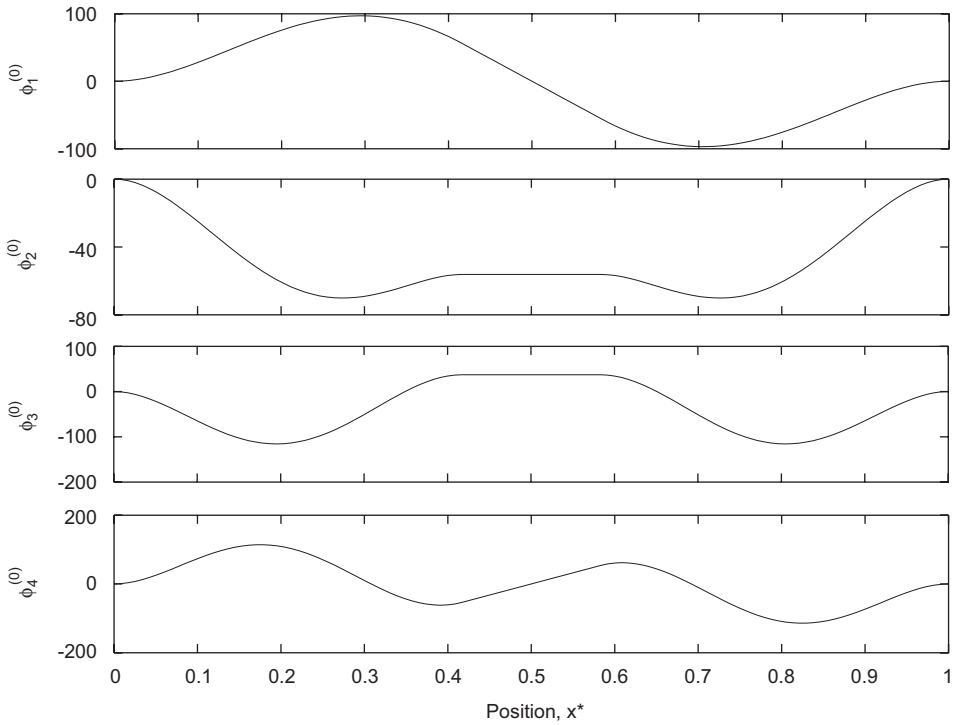

Fig. 3. First four normalized mode shapes in $S^{(1)}$; $\omega_i^* = 3.46$, 5.75, 9.14, and 11.11. Parameters are as listed in Table 1; $k^* = 10^5$.

Motion of the rigid body and attached beams in $S^{(j)}$ is a superposition of N modal vectors $\underline{\phi}^{(j)}$, written as

$$\underline{u}^{(j)}(x,t) \approx \sum_{i=1}^{N} \eta_i^{(j)}(t)\underline{\phi}_i^{(j)}(x), \tag{18}$$

where the $\eta_i^{(j)}(t)$ are generalized coordinates in the discretization. Motion within either state is described fully by the sets $\{\eta_i^{(j)}\}$, and the remaining portion of the contact analysis involves a mapping between those two sets for each contact event. In the light of orthogonality among the $\underline{\phi}^{(j)}$, each modal coordinate satisfies

$$\ddot{\eta}_i^{(j)} + 2\xi^{(j)}\omega_i\dot{\eta}_i^{(j)} + \omega_i^2\eta_i^{(j)} = \langle \underline{f}, \underline{u}_i^{(j)} \rangle, \tag{19}$$

where $\xi^{(j)}$ is the modal damping ratio for the system in state j. Accounting for the prescribed base motion, the particular solution takes the form $Q_i^{(j)}\sin(\omega t) + R_i^{(j)}\cos(\omega t)$. With the system's initial displacement $\underline{u}_o$ and velocity $\dot{\underline{u}}_o$ vectors known, the modal coordinates $\eta_i^{(j)}$ are calculated as outlined in the Appendix.

4. Mapping between states

Switching between states occurs when there is impact between the rigid body and base, or loss-of-contact between the two, and at those conditions

$$w_1(L_1,t) + aw_{1,x}(L_1,t) + c = 0. \tag{20}$$

Should the spring be located at the center of the rigid body ($a = L_m/2$), then this condition simplifies to $y + c = 0$. The roots of Eq. (20) identify the instants at which the body contacts the spring or rebounds from it.

With a specific impact or rebound time being denoted by t_k as shown in Fig. 4, the displacement and velocity of the system just beforehand (t_k^-) are related to those just afterwards (t_k^+) by enforcing compatibility conditions [16]. For impact at t_k and rebound at t_{k+1},

$$\begin{aligned} \text{Impact:} \quad & \underline{u}^{(0)}(x,t_k^-) = \underline{u}^{(1)}(x,t_k^+), \\ & \dot{\underline{u}}^{(0)}(x,t_k^-) = \dot{\underline{u}}^{(1)}(x,t_k^+). \\ \text{Rebound:} \quad & \underline{u}^{(1)}(x,t_{k+1}^-) = \underline{u}^{(0)}(x,t_{k+1}^+), \\ & \dot{\underline{u}}^{(1)}(x,t_{k+1}^-) = \dot{\underline{u}}^{(0)}(x,t_{k+1}^+). \end{aligned} \tag{21}$$

The continuity conditions at impact require that the two sets of modal coordinates are related by

$$\begin{aligned} \underline{\eta}^{(1)}(t_k^+) &= \underline{T}^{(01)}\underline{\eta}^{(0)}(t_k^-), \\ \dot{\underline{\eta}}^{(1)}(t_k^+) &= \underline{T}^{(01)}\dot{\underline{\eta}}^{(0)}(t_k^-), \end{aligned} \tag{22}$$

where $\underline{\eta}^{(j)}$ is a column vector comprising the $\eta_i^{(j)}$. The transformation matrix $\underline{T}^{(01)}$ is constant, and it is determined solely by the sets of eigenfunctions in $S^{(j)}$. The p–q element of $\underline{T}^{(01)}$ is the $\underline{M}$-weighted projection of modal vectors in the two bases:

$$\begin{aligned} \underline{T}_{p,q}^{(01)} &= \langle \underline{M}\,\underline{\phi}_q^{(0)}, \underline{\phi}_p^{(1)} \rangle \\ &= \int_0^{L_1} \rho_1 A_1 W_{1q}^{(0)} W_{1p}^{(1)}\,\mathrm{d}x_1 + \int_0^{L_2} \rho_2 A_2 W_{2q}^{(0)} W_{2p}^{(1)}\,\mathrm{d}x_2 \\ &\quad + m Y_q^{(0)} Y_p^{(1)} + J\Theta_q^{(0)}\Theta_p^{(1)}. \end{aligned} \tag{23}$$

The companion matrix $\underline{T}^{(10)} = \underline{T}^{(01)\mathrm{T}}$ maps rebound from $S^{(1)}$ to $S^{(0)}$.

Figs. 4 and 5 illustrate maps between the two sets of modal coordinates. Fig. 4(a) depicts a period-one (P-1) steady-state response, in which one impact and one rebound occur during each oscillation of the structure's base. Linear vibration occurs in $S^{(0)}$ with the modal coordinates $\eta_i^{(0)}$ evolving according to Eq. (19); $\underline{T}^{(01)}$ maps $\underline{\eta}^{(0)}$ to $\underline{\eta}^{(1)}$ across the impact at t_k; linear vibration occurs in $S^{(1)}$ with the modal coordinates $\eta_i^{(1)}$ evolving

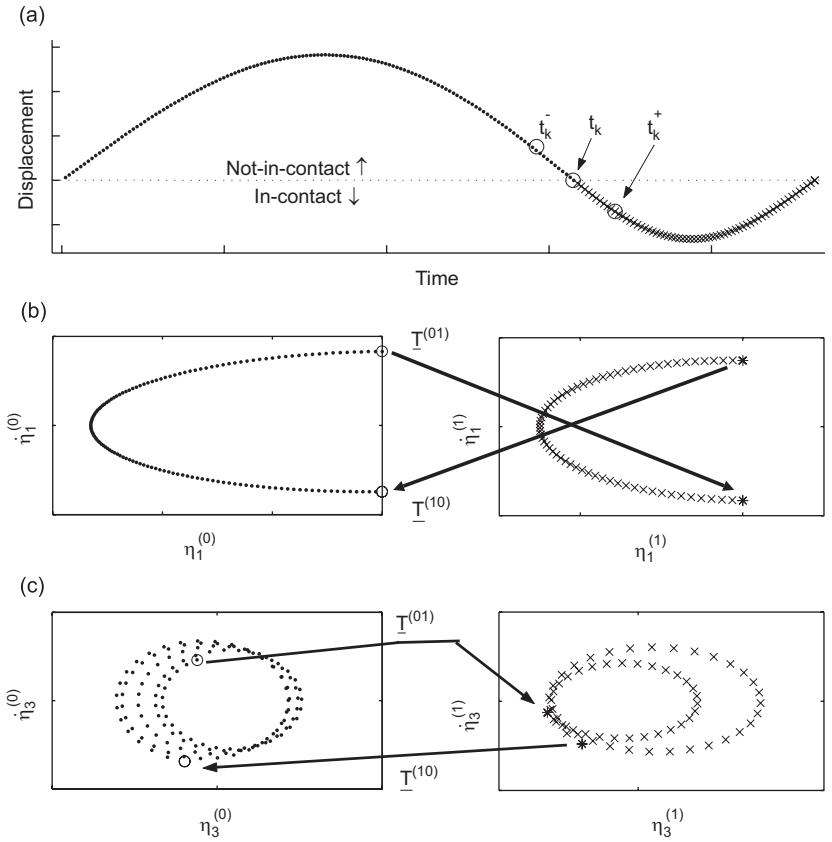

Fig. 4. Schematic illustration of the mapping across impact at t_k for a period-one response. (a) Displacement of the rigid body's mass center ($n = 1$ peak, $\omega^* = 1.355$). (b) Modal coordinate trajectories and mapping between $\eta_1^{(0)}$ and $\eta_1^{(1)}$. (c) Modal coordinate trajectories and mapping between $\eta_3^{(0)}$ and $\eta_3^{(1)}$. Here $k^* = 10^4$, $N = 8$ for each state, $\xi^{(0)} = 1\%$, and $\xi^{(1)} = 5\%$. Trajectories in $S^{(0)}$ are denoted by $(\cdots)$, and those in $S^{(1)}$ by $(\times\times\times)$.

according to Eq. (19); and $\underline{T}^{(10)}$ maps $\underline{\eta}^{(1)}$ back to $\underline{\eta}^{(0)}$ across impact at t_{k+1}. The corresponding paths traced by $\eta_1^{(0)}$ and $\eta_1^{(1)}$ in their respective state spaces are shown in Fig. 4(b), along with the transformations between them. During this cycle, the $\eta_3^{(0)}$ and $\eta_3^{(1)}$ coordinates in Fig. 4(c) undergo multiple oscillations in the light of their higher frequencies.

Fig. 5(a) depicts a more-complex period-three (P-3) motion including impacts, rebounds, and grazing contact. During a time interval corresponding to three oscillations of the table's base, the rigid body and beam system moves freely, contacts the spring, loses contact, and then contacts it again over approximately the last third of a cycle. The maps transform modal coordinates for each of the two impacts and two rebounds: $\underline{T}^{(01)}$ for the transitions labeled B–C and F–G, and $\underline{T}^{(10)}$ for the transitions D–E and H–A.

5. Results and discussion

For a single-degree-of-freedom system, the oscillator's peak displacement between successive impacts is a convenient scalar metric of the steady-state response's amplitude [5]. When viewed as a function of the excitation frequency, that quantity is a useful measure for describing the repetitive impact frequency response function. For the continuous system at hand, the displacement varies along the structure, multiple frequencies are present, and multiple modes contribute to that response.[1] In what follows, the dimensionless impulse

[1]For generality, the subsequent results are presented entirely in dimensionless form, and non-dimensional parameters are denoted by an asterisk superscript. Time is non-dimensionalized with respect to the structure's fundamental natural frequency in $S^{(0)}$ such that $t^* = \omega_1^{(0)} t$. Displacements are normalized by the total length L.

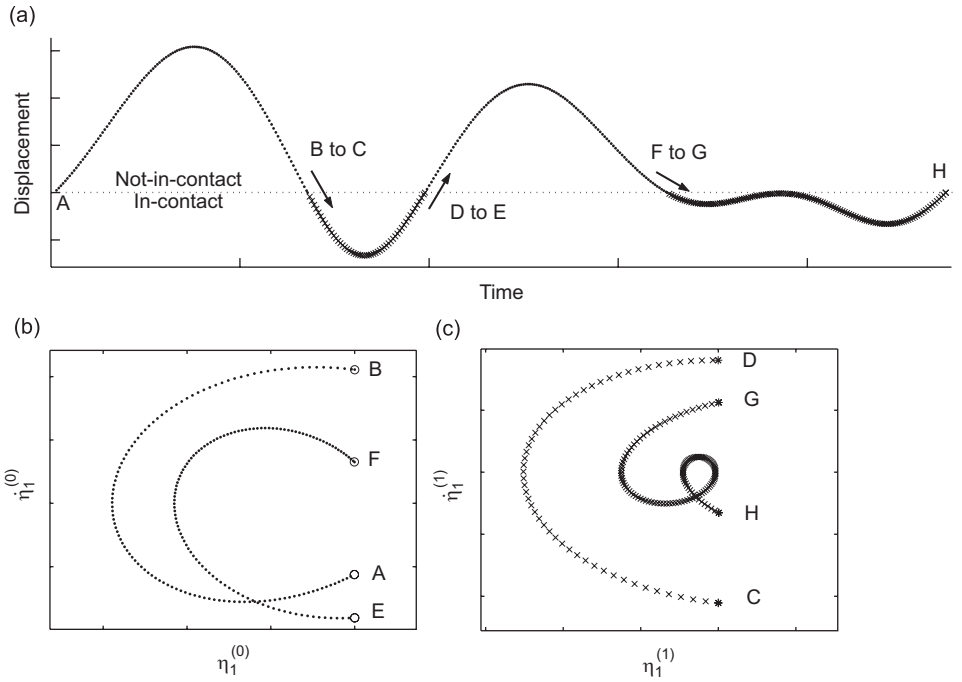

Fig. 5. Schematic illustration of the mapping across impact at t_k for a period-three response. (a) Displacement of the rigid body's mass center ($\omega^* = 2$). Modal coordinate trajectories and mapping between (b) $\eta_1^{(0)}$ and (c) $\eta_1^{(1)}$. Here $k^* = 10^4$, $N = 8$ for each state, $\xi^{(0)} = 1\%$, and $\xi^{(1)} = 5\%$. Trajectories in $S^{(0)}$ are denoted by $(\cdots)$, and those in $S^{(1)}$ by $(\times\times\times)$.

$I^* = (I\omega_1^{(0)})/(k_b L)$ (where I is the dimensional value) exerted on the rigid body during contact is taken to represent the character of response as a function of excitation frequency.

The frequency response of a repetitive impact oscillator can have periodic, quasi-periodic, or chaotic behavior. Simulations of the rigid body and beam system at hand exhibit a number of qualitatively different features in the frequency response, including multiple harmonics at which local resonance occurs, bifurcations in amplitude, and instances of grazing impact. Such phenomena have been observed in the context of other nonlinear structures. Shaw and Holmes [5] identified flip bifurcations, which are sudden changes in periodicity occurring along a branch of the frequency response function. A supercritical flip bifurcation occurs when a branch corresponding to a period-one response splits into two branches, which together mark the paired amplitudes of period-two vibration. Sudden changes in the response period for small changes in the driving frequency can also occur. For instance, a period-m branch can jump to a period-n response with small frequency changes, a phenomenon that is manifested as an apparent jump or discontinuity in the frequency response function. Such discontinuities were examined in the context of hysteretic effects by Minorsky [17] among others. Cascades of period-doubling bifurcations were examined by Narayanan and Sekar [9], who demonstrated the existence of crossed branches in the spectrum of a damped single-degree-of-freedom system. A grazing impact occurs when contact between surfaces is imminent, but the contact impulse at that borderline condition vanishes [18]. The study of de Weger et al. [19] applied perturbation methods to study grazing phenomena and disclosed discontinuities and overlapping regions in the frequency response function.

5.1. Discretization and relative convergence

The model is discretized in Eq. (18) through the subset of N modes in each of the two states $S^{(j)}$. The fidelity of the approximation is assessed by relative convergence of the repetitive impact frequency response function as a function of N, recognizing the trade-off involved between computational efficiency and accuracy of the simulation over a particular frequency range.

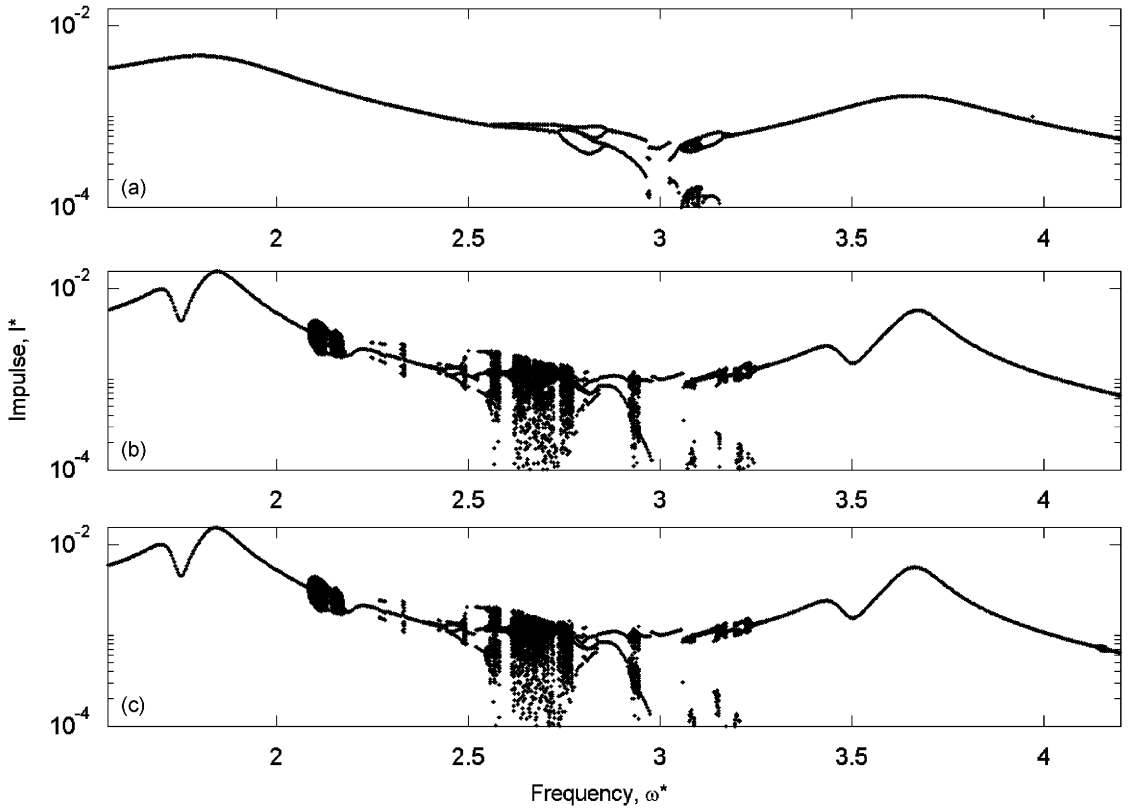

Fig. 6. Relative convergence of the repetitive impact frequency response function in terms of the number of modes N taken in the structure's discretization for each $S^{(j)}$: (a) $N = 2$, (b) $N = 4$, and (c) $N = 6$. Here $k^* = 3 \times 10^5$, $\xi^{(0)} = 1\%$, and $\xi^{(1)} = 5\%$.

In Fig. 6(a), the repetitive impact frequency response function is shown for the parameters listed in Table 1 and with $N = 2$. Broad and isolated peaks occur near $\omega^* = 1.8$ and 3.6, and a narrow region comprising the complex dynamics of loops and discontinuities occurs over $2.55 < \omega^* < 3.25$. However, that spectrum is predicted on the basis of a two-mode approximation in $S^{(0)}$ (as in Fig. 2), and a two-mode approximation in $S^{(1)}$ (as in Fig. 3). In Fig. 6(b) with $N = 4$, two closely spaced peaks develop at $\omega^* = 1.70$ and 1.84, in contrast to the single peaks present in the $N = 2$ model. A similar pair develops across $\omega^* = 3.5$. Further, the simpler two-mode approximation does not capture the more complex features associated with mode-to-mode coupling that are evident over $2.08 < \omega^* < 3.25$. The additional complexity at $N = 4$ includes discontinuities, the loop structure at $2.08 < \omega^* < 2.18$, and a broad region of apparent chaos. At $N = 6$ in Fig. 6(c), the frequency response function changes slightly relative to the solution at $N = 4$ over this frequency range. In what follows, $N = 8$ is taken as a compromise between computational efficiency and relative convergence in such spectra.

5.2. Harmonic structures

The repetitive impact frequency response function includes a number of features that occur at regular frequency intervals, either integer or fractional multiples of a fundamental frequency. Fig. 7(a) illustrates the frequency response of a system having relatively low modal damping and contact stiffness. By way of nomenclature in describing such functions, the integer n denotes the nth harmonic, and represents a motion that has period n relative to the excitation. The corresponding time history for displacement of the rigid body's centroid at the $n = 1$ resonance peak in Fig. 7(a) is shown in Fig. 8(a). In this period-one response, for each cycle of base motion $e(t)$, the structure also completes one cycle in the steady state. With a local resonant

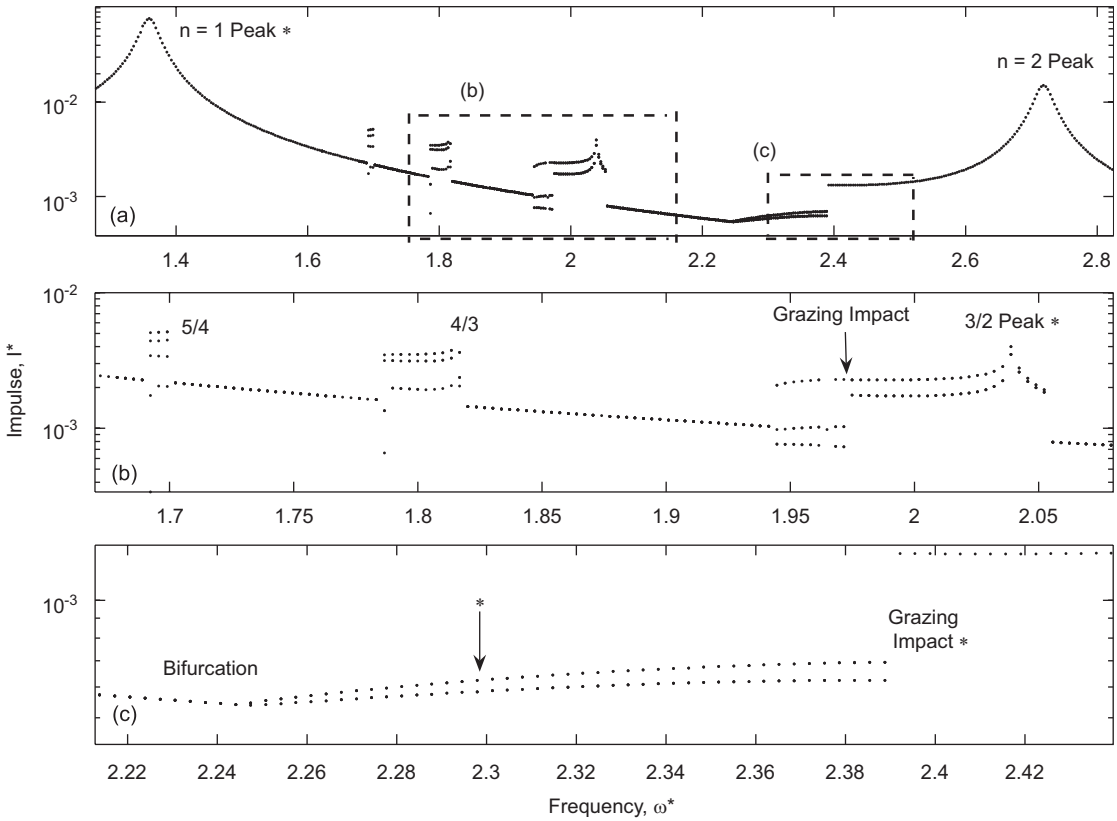

Fig. 7. Repetitive impact frequency response function with $k^* = 10^4$, $\xi^{(0)} = 1\%$, and $\xi^{(1)} = 1\%$. (a) Response over a broad frequency range encompassing the $n = 1$ peak and its second harmonic. The regions within the dashed borders are magnified in subfigures (b) and (c). (b) Magnified view of the region in which fractional harmonics are present. (c) Magnified view of the region in which the period-one to period-two bifurcation occurs, and in which a discontinuity develops through a grazing impact. Responses $y^*(t)$ at the conditions identified by the $(*)$ notation are shown in Fig. 8.

frequency of $\omega^* = 1.36$, the $n = 1$ peak falls between the first natural frequencies ($\omega^* = 1$ and 2.12) of the system in its states $S^{(j)}$. Also in Fig. 7(a), the harmonics of this peak appear in the spectrum, but with decreasing amplitudes; the labeled $n = 2$ peak occurs at exactly twice the frequency of the $n = 1$ peak, but with only 20% of its amplitude.

At the relatively low dissipation level of Fig. 7, intermediate peaks develop between the integer-spaced harmonics; these fractional harmonics occur at ratios 3/2, 4/3, 5/4... $m/(m-1)$, for $m = 3$ and higher, of the $n = 1$ peak. In analogous single-degree-of-freedom studies, intermediate peaks have been shown to occur at exactly the half-harmonic locations, and for a continuous system, the intermediate peaks can cascade to ratios less than half [13]. The $m/(m-1)$ harmonics tend toward an accumulation point at the $n = 1$ peak. However, the higher fractional harmonics diminish in width and amplitude with additional damping; in Fig. 7(b), the three harmonics $m = 3$, 4, and 5 are present at the chosen value of 1% modal damping.

The resonances corresponding to fractional harmonics extend over small ranges in the impact frequency response function. The time history for $y^*(t)$ at the 3/2-harmonic in Fig. 7(b) is depicted in Fig. 8(b). Here the base undergoes three complete cycles, while the rigid body has only two local maxima in $S^{(0)}$ (and two local minima in $S^{(1)}$). The width in frequency of these regions decreases with m; in Fig. 7(b), for instance, the region corresponding to the 4/3-harmonic is only approximately 30% as wide as that of the 3/2-harmonic, a result consistent with the findings of Gontier and Toulemonde [7]. Likewise, as dissipation increases, the magnitudes and widths of the fractional peaks decrease. In Fig. 9, the structure's frequency response was simulated over a range of modal damping $\xi^{(j)}$. Fig. 9 also illustrates how only two fractional harmonics ($m = 3$ and 4) are

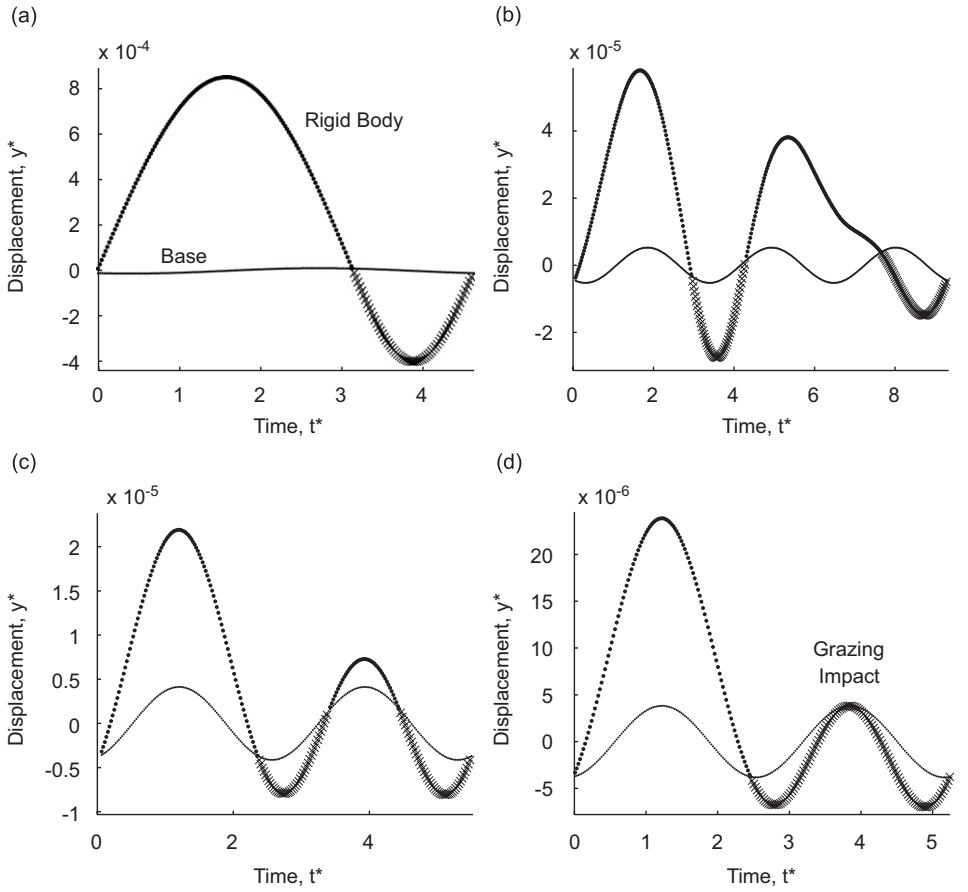

Fig. 8. Time histories for the rigid body's non-dimensional displacement $y(t)$ at the conditions designated by the (*) notation in Fig. 7. (a) Response at the $n = 1$ peak ($\omega^* = 1.36$). (b) Response at the 3/2-fractional harmonic peak ($\omega^* = 2.04$). (c) Response subsequent to the period-two bifurcation ($\omega^* = 2.30$). (d) Response subsequent to the grazing impact discontinuity ($\omega^* = 2.39$). Absolute motions in $S^{(0)}$ are denoted by $(\cdots)$, and those in $S^{(1)}$ by $(\times\times\times)$. The displacement of the structure's base is denoted by (—).

present at $\xi^{(1)} = 2\%$ in response to additional dissipation. No fractional harmonics develop at $\xi^{(1)} = 15\%$, and even at $\xi > 10\%$, they are nearly indiscernible.

The magnitude of the contact stiffness likewise has qualitative implications for the complexity of the repetitive impact frequency response function. With damping now held constant in Fig. 10, changes in k^* significantly alter the structure of harmonic peaks, fractional peaks, bifurcation points, and regions of apparent chaos [12]. At the relatively low value $k^* = 10^4$ in Fig. 10(a), a single period-one peak occurs at $\omega^* = 1.36$, and its period-two harmonic is present at $\omega^* = 2.72$. As the stiffness increases beyond $k^* = 6 \times 10^4$, the single $n = 1$ peak pairs with another at a slightly higher frequency. For instance, at $k^* = 10^5$ in Fig. 10(b), two peaks emerge at $\omega^* = 1.68$ and 1.79, as well as their second harmonics. For $k^* > 1.7 \times 10^5$, the magnitude of the second peak in the pair grows beyond that of the first generating peak. Fig. 10(c) illustrates that phenomenon at $k^* = 3 \times 10^5$, where the peak at $\omega^* = 1.84$ is 52% larger in amplitude than the peak at $\omega^* = 1.70$. In addition to these changes in the n-peak structure, the repetitive impact frequency response functions increase substantially in complexity at intermediate values.

5.3. Bifurcations

The character of the P-1 to P-2 bifurcation highlighted in Fig. 7(c) depends on the level of modal dissipation. While damping has little influence on the frequency at which the bifurcation occurs, it does affect the width and separation of the two subsequent branches. Comparing the bifurcations for the cases of 2% and

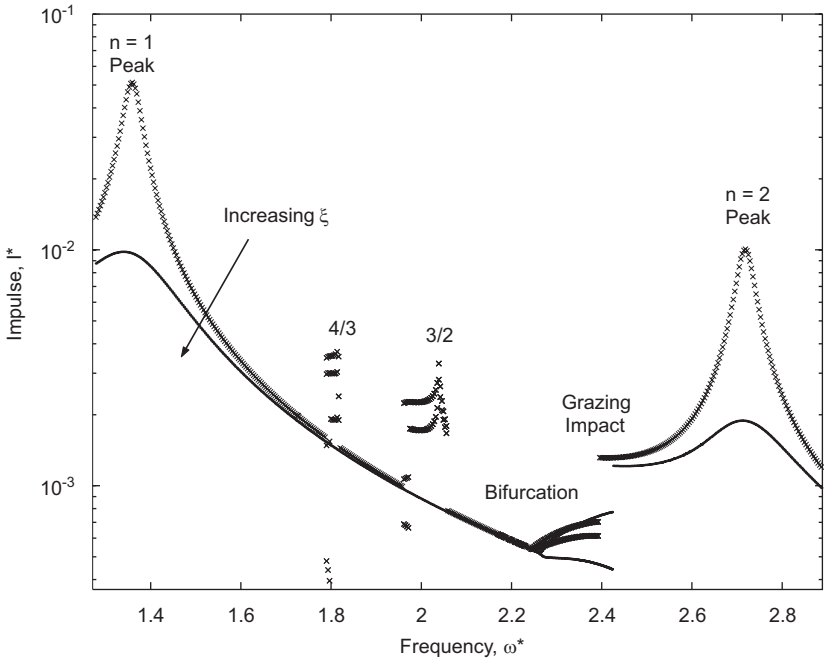

Fig. 9. Effect of dissipation on the structure of the repetitive impact frequency response function, particularly the local resonance peaks n and fractional harmonics m. Here $k^* = 10^4$ and $\xi^{(0)} = 1\%$. The responses for $\xi^{(1)} = 2\%$ ($\times\times\times$) and $\xi^{(1)} = 15\%$ ($\cdots$) are superimposed.

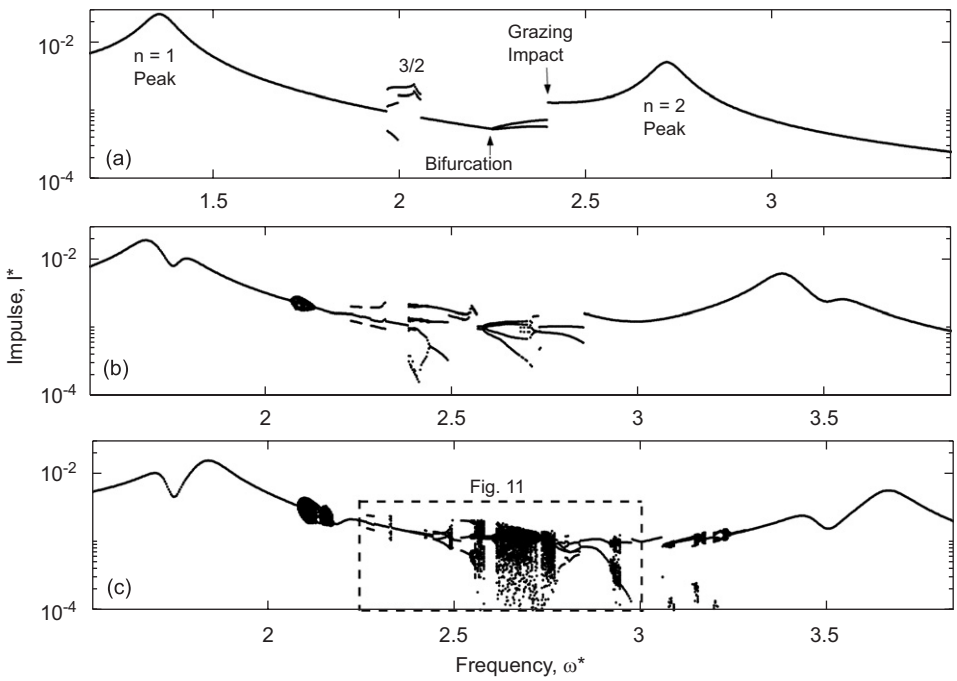

Fig. 10. Effect of contact stiffness on the structure of the repetitive impact frequency response function, particularly the local resonance peaks n, fractional harmonics m, bifurcations, and regions of apparent chaos. Here $\xi^{(0)} = 1\%$ and $\xi^{(1)} = 5\%$. Responses at (a) $k^* = 10^4$, (b) $k^* = 10^5$, and (c) $k^* = 3 \times 10^5$.

15% modal damping in Fig. 9, the splits occur at the virtually the same locations, with the branch-point frequency increasing by only 0.45% between $\xi = 2\%$ and 15%. The separation between these branches at $\xi = 15\%$ immediately prior to the grazing impact condition is 365% greater than that for $\xi = 2\%$. In short, the length, breadth, and branch-point frequency of the period-one to period-two bifurcations each increase with ξ, albeit to different extents.

5.4. Grazing impact

Figs. 8(c) and (d) also depict the time histories associated with the transition between the direct and grazing impacts in Fig. 7(c). In the former case, the P-2 motion comprises two local maxima in $S^{(0)}$, and two local minima in $S^{(1)}$, so that two collisions occur for each complete cycle. Subsequent to the onset of a grazing impact at $\omega^* = 2.39$, the response remains P-2, but with only one local maximum in $S^{(0)}$.

Grazing impact or rebound results in a distinct discontinuity in the repetitive impact frequency response function, as highlighted in Figs. 7(c) and 9. With a slight increase in ω^*, the two post-bifurcation branches abruptly terminate, and a single locus of greater magnitude develops subsequently. The motion of the system, as measured by the displacement time record $y^*(t)$, does not change appreciably over this slight change in frequency.

5.5. Aggregate response

For lower values of the contact stiffness, the repetitive impact frequency response function comprises a pattern of flip bifurcations, grazing impacts and rebounds, and a series of fractional harmonics (for sufficiently low dissipation). As the stiffness increases, the response function becomes generally more complex. For instance, the region associated with the 3/2-fractional harmonic peak in Fig. 7(b) also contains a grazing impact. At $\omega^* = 1.944$, three P-3 branches generate from a single P-1 branch in the response function. Those branches subsequently coalesce to two branches through grazing impact at $\omega^* = 1.973$.

The additional grazing impact in this region develops through relatively low contact stiffness, as in Fig. 10(a). At higher stiffness values, the discontinuities overlay into the complex response spectrum shown in Fig. 11 for $k^* = 3 \times 10^5$. Here, the fractional harmonics, bifurcations, and grazing impacts are no longer

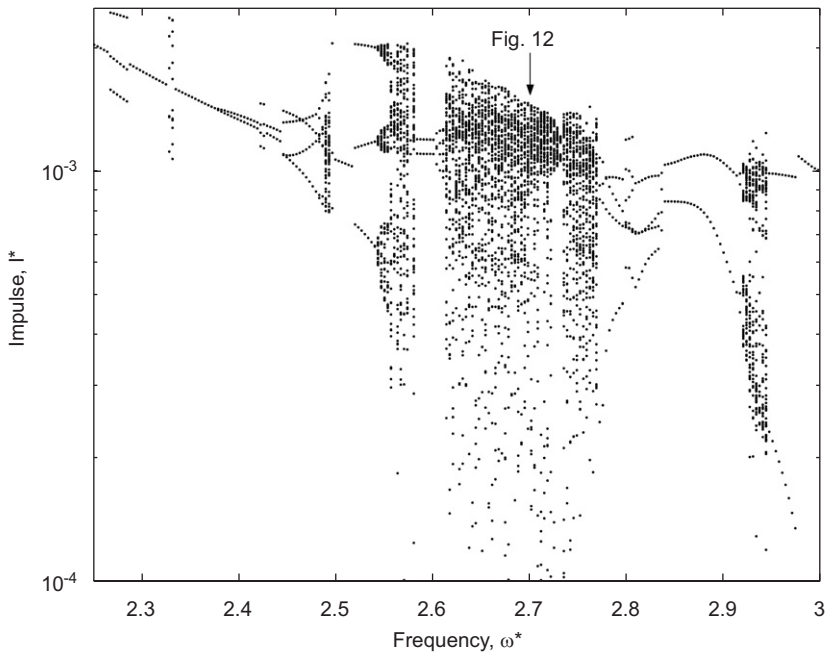

Fig. 11. Magnified view of the repetitive impact frequency response function having complex dynamics. Here $k^* = 3 \times 10^5$, $\xi^{(0)} = 1\%$, and $\xi^{(1)} = 5\%$.

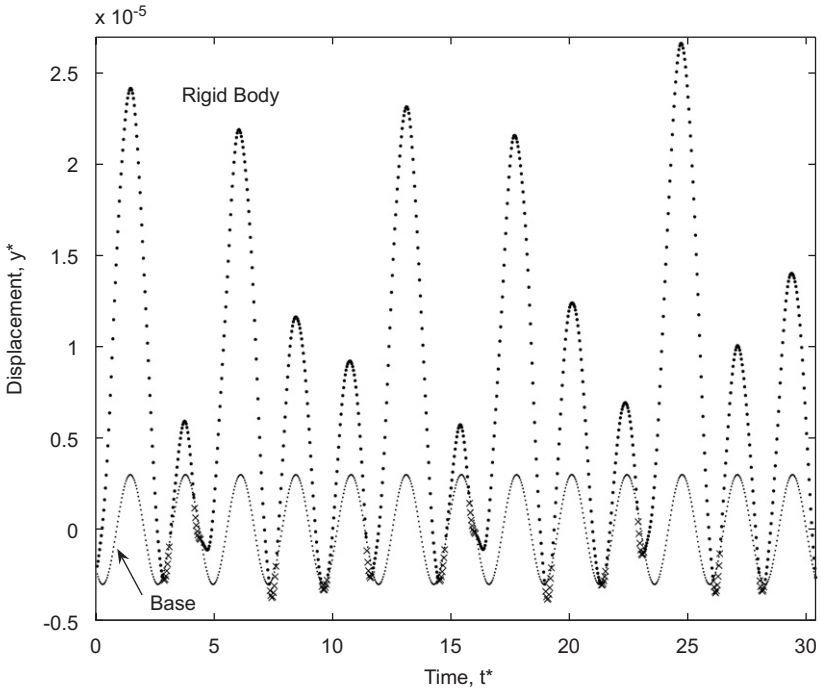

Fig. 12. Apparently chaotic time history $y^*(t)$ of the response identified in Fig. 11; $\omega^* = 2.70$. Absolute motions in $S^{(0)}$ are denoted by $(\cdots)$, and those in $S^{(1)}$ by $(\times\times\times)$.

individually discernible, and bounded bands of apparently chaotic behavior are also present. An illustrative time record for one such band is shown in Fig. 12, and steady-state response is not reached even after thousands of impacts.

6. Influence of asymmetry

The structure's natural frequencies and mode shapes are sensitive to symmetry in the model. The introduction of asymmetry, in geometry or the point of contact, shifts the peaks and qualitative character of the repetitive impact frequency response function. In addition, the degree of overall complexity changes with asymmetry.

The parameter a determines the location of contact on the rigid body. When $a = L_m/2$, only the $S^{(1)}$ symmetric modes in Fig. 3 are excited through contact. For $a = 0$ and $a = L_m/4$, the $S^{(1)}$ anti-symmetric modes are also driven, and additional modes are required in the discretization for acceptable convergence. For different values of a, the $n = 1$ peak and its second harmonic are identically located, and as $a \to 0$, the amplitudes of these peaks decrease. Fig. 13 illustrates the influence of offset on a complex response in the region between the $n = 1$ and 2 peaks. As Figs. 13(a)–(c) indicate, the region $\omega^* \in (1.70, 2.44)$ is particularly rich and increases in complexity as the spring's location shifts, or as $a \to 0$.

Fig. 14 shows frequency response diagrams for three values of h_1. For the symmetric case in which the beams have the same thicknesses (Fig. 14(b)), the harmonic peaks, the 3/2-fractional harmonic peak, the period-one to period-two bifurcation, and the grazing impact features have a structure similar to that discussed above. For the case in which beam "1" is less stiff than beam "2" (Fig. 14(a)), the width of the 3/2-fractional harmonic region grows even to the point of coalescence with the bifurcation region near $\omega^* = 2.38$. Alternatively, when beam "1" is twice as high as and thus more stiff than beam "2" (Fig. 14(c)), no fractional harmonics appear. In this case, the complexity of the frequency response diagram decreases as the structure becomes less symmetric and stiffer.

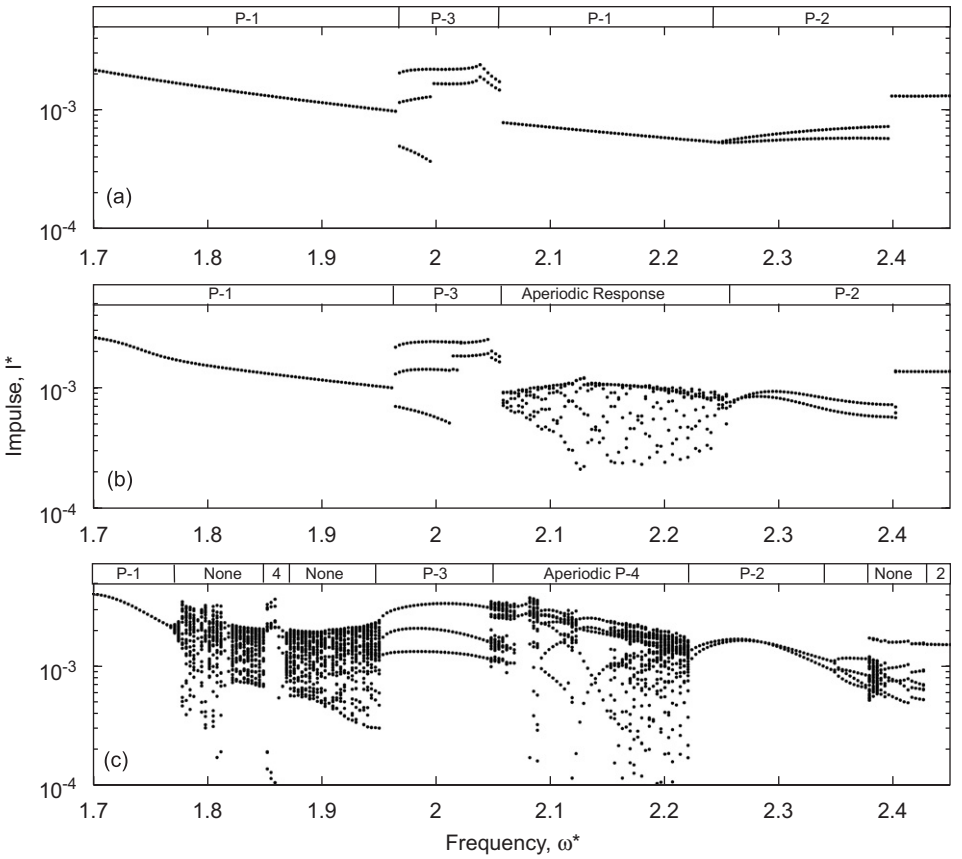

Fig. 13. Contribution of offset to the structure of the repetitive impact frequency response function; $\xi^{(0)} = 1\%$, $\xi^{(1)} = 5\%$, $c^* = 0$, and N = 12. The magnified views are shown between the $n = 1$ and $n = 2$ harmonic peaks for conditions (a) a $= L_m/2$, (b) a $= L_m/4$, and (c) a $= 0$.

7. Summary

The vibration of a beam and rigid body system that can contact a base structure, with impact modeled by the linear restoring force of a spring, is examined. This type of structure, the excitation means, and the response complexity are relevant to the design and operation of mechanical systems that are subjected to repetitive impact, and in particular, to some internal components present in nuclear reactor power plants.

The motion is described in a piecewise fashion as switching between the in-contact and not-in-contact states, and compatibility conditions are applied at their junctions. The equations of motion for the beam and rigid body are cast in an extended state operator format, so that modal analysis can be applied within each state. Those solutions are stitched together sequentially to form and to study the steady state response. The two sets of modal coordinates (in-contact and not-in-contact) are related across the instantaneous contact and loss-of-contact events by transformation matrices which are calculated in terms of the mass-weighted projection of one set of mode shapes onto another.

The simulation method is computationally efficient, even when multiple modes are included in discretization. The predicted repetitive impact frequency response functions capture the rich dynamics of the structure, and they are expressed in terms of the contact's impulse. Fig. 7, for instance, demonstrates the presence of multiple harmonics, fractional harmonics, bifurcations, and grazing impacts. Parameter studies investigate the influence of dissipation (Fig. 9), contact stiffness (Fig. 10), and asymmetry (Fig. 13) on the complexity of the structure's frequency response.

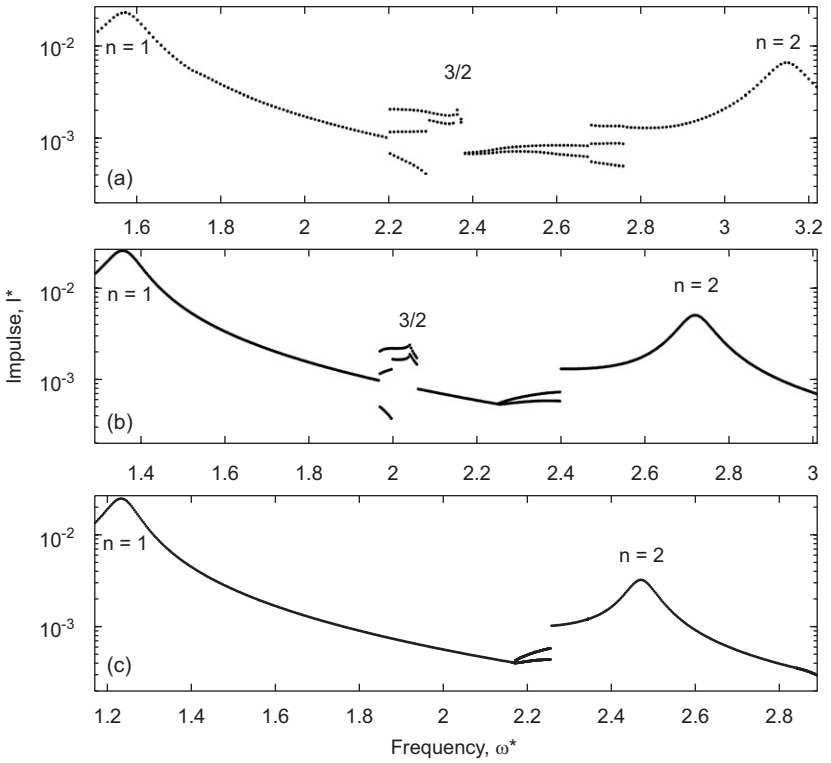

Fig. 14. Effect of the relative beam-rigid body impedance ratio on the repetitive impact frequency response function; $\xi^{(0)} = 1\%$, $\xi^{(1)} = 5\%$, and $c^* = 0$. The responses are shown for h_1 values (a) half, (b) equal to, and (c) twice the nominal value listed in Table 1.

Appendix A

Provided herein are the expressions relating to the mapping within a state, as discussed in Section 3. These expressions apply for any time t and for either $S^{(0)}$ or $S^{(1)}$, using the particular solution coefficients $Q_i^{(j)}$ and $R_i^{(j)}$ obtained from Eq. (19) in terms of the shifted time $\Delta t = t - t_k^+$. For a given mode i having a natural frequency ω_i and damped natural frequency $\omega_d = \sqrt{1-\xi^2}\omega_i$, the modal coordinates evolve according to

$$\begin{bmatrix} \eta_i^{(j)}(t) \\ \dot{\eta}_i^{(j)}(t) \end{bmatrix} = \frac{e^{-\xi\omega_i}}{\sqrt{1-\xi^2}} \begin{bmatrix} \xi\sin(\omega_d\Delta t) + \sqrt{1-\xi^2}\cos(\omega_d\Delta t) & \frac{1}{\omega_i}\sin(\omega_d\Delta t) \\ -\omega_i\sin(\omega_d\Delta t) & -\xi\sin(\omega_d\Delta t) + \sqrt{1-\xi^2}\cos(\omega_d\Delta t) \end{bmatrix} \times \begin{bmatrix} \eta_i^{(j)}(t_k^+) \\ \dot{\eta}_i^{(j)}(t_k^+) \end{bmatrix} + \begin{bmatrix} F_{11}(\omega,\omega_i,t,t_k^+,\xi) & F_{12}(\omega,\omega_i,t,t_k^+,\xi) \\ F_{21}(\omega,\omega_i,t,t_k^+,\xi) & F_{22}(\omega,\omega_i,t,t_k^+,\xi) \end{bmatrix} \begin{bmatrix} Q_p^{(j)}(t_k^+) \\ R_p^{(j)}(t_k^+) \end{bmatrix}, \tag{A.1}$$

where

$$F_{11} = \sin(\omega t) - e^{\xi\omega_i\Delta t}\frac{\omega}{\omega_d}\cos(\omega t_k^+)\sin(\omega_d\Delta t) - e^{\xi\omega_i\Delta t}\frac{\xi}{\sqrt{1-\xi^2}}\sin(\omega t_k^+)\sin(\omega_d\Delta t) - e^{\xi\omega_i\Delta t}\sin(\omega t_k^+)\cos(\omega_d\Delta t),$$

$$F_{12} = \cos(\omega t) + e^{\xi\omega_i\Delta t}\frac{\omega}{\omega_d}\sin(\omega t_k^+)\sin(\omega_d\Delta t) - e^{\xi\omega_i\Delta t}\frac{\xi}{\sqrt{1-\xi^2}}\cos(\omega t_k^+)\sin(\omega_d\Delta t) - e^{\xi\omega_i\Delta t}\cos(\omega t_k^+)\cos(\omega_d\Delta t),$$

$$
\begin{aligned}
F_{21} = {} & \omega\cos(\omega t) - e^{\xi\omega_i\Delta t}\xi\omega_i\sin(\omega t_k^+)\cos(\omega_d\Delta t) + e^{\xi\omega_i\Delta t}\frac{\xi^2}{\sqrt{1-\xi^2}}\omega_i\sin(\omega t_k^+)\sin(\omega_d\Delta t) \\
& - e^{\xi\omega_i\Delta t}\omega\cos(\omega t_k^+)\cos(\omega_d\Delta t) + e^{\xi\omega_i\Delta t}\frac{\xi}{\sqrt{1-\xi^2}}\sin(\omega_d\Delta t)\omega\cos(\omega t_k^+) \\
& + e^{\xi\omega_i\Delta t}\sin(\omega t_k^+)\sqrt{1-\xi^2}\omega_i\sin(\omega_d\Delta t) + e^{\xi\omega_i\Delta t}\sin(\omega t_k^+)\xi\omega_i\cos(\omega_d\Delta t),
\end{aligned}
$$

$$
\begin{aligned}
F_{22} = {} & -\omega\sin(\omega t) - e^{\xi\omega_i\Delta t}\xi\omega_i\cos(\omega t_k^+)\cos(\omega_d\Delta t) + e^{\xi\omega_i\Delta t}\omega_i\frac{\xi^2}{\sqrt{1-\xi^2}}\sin(\omega_d\Delta t)\cos(\omega t_k^+) \\
& + e^{\xi\omega_i\Delta t}\omega\sin(\omega t_k^+)\cos(\omega_d\Delta t) - e^{\xi\omega_i\Delta t}\omega\frac{\xi}{\sqrt{1-\xi^2}}\sin(\omega_d\Delta t)\sin(\omega t_k^+) \\
& + e^{\xi\omega_i\Delta t}\omega_d\cos(\omega t_k^+)\sin(\omega_d\Delta t) + e^{\xi\omega_i\Delta t}\xi\omega_i\cos(\omega_d\Delta t)\cos(\omega t_k^+). \qquad \text{(A.2)}
\end{aligned}
$$

References

[1] S.-H. Cho, S.-T. Ahn, Y.-H. Kim, A simple model to estimate the impact force induced by piston slap, *Journal of Sound and Vibration* 252 (2002) 229–242.

[2] K.P. Duffy, R.L. Bagley, O. Mehmed, On a self-tuning impact vibration damper for rotating turbomachinery, *American Institute of Aeronautics and Aerospace Joint Propulsion Conference*, AIAA-2000-3100, NASA TM-2000-210215, 2000.

[3] Anonymous, Issues stemming from NRC staff review of recent difficulties experienced in maintaining steam generator tube integrity, United States Nuclear Regulatory Commission, Regulatory Issue Summary 2000-022, 2000.

[4] Anonymous, Fuel review: design data, *Nuclear Engineering International* 49 (602) (2004) 26–355.

[5] S.W. Shaw, P.J. Holmes, A periodically forced piecewise linear oscillator, *Journal of Sound and Vibration* 90 (1983) 129–155.

[6] S. Maezawa, H. Kumano, Y. Minakuchi, Forced vibrations in an unsymmetrical piece-wise linear system excited by general periodic force function, *Bulletin of the Japan Society of Mechanical Engineers* 23 (1980) 68–75.

[7] C. Gontier, C. Toulemonde, Approach to the periodic and chaotic behaviour of the impact oscillator by a continuation method, *European Journal of Mechanics: A/Solids* 16 (1997) 141–163.

[8] Y.B. Kim, S.T. Noah, Stability and bifurcation analysis of oscillators with piecewise-linear characteristics: a general approach, *American Society of Mechanical Engineers Journal of Applied Mechanics* 58 (1991) 545–553.

[9] S. Narayanan, P. Sekar, Periodic and chaotic responses of an SDF system with piecewise linear stiffness subjected to combined harmonic and flow induced excitations, *Journal of Sound and Vibration* 184 (1995) 281–298.

[10] R.G. Parker, P.J. Sathe, Free vibration and stability of a spinning disk-spindle system, *Journal of Vibration and Acoustics* 121 (1999) 391–396.

[11] J. Knudsen, A.R. Massih, Dynamic stability of weakly damped oscillators with elastic impacts and wear, *Journal of Sound and Vibration* 263 (2003) 175–204.

[12] L. Xu, M.W. Lu, Q. Cao, Nonlinear vibrations of dynamical systems with a general form of piecewise-linear viscous damping by incremental harmonic balance method, *Physics Letters A* 301 (2002) 65–73.

[13] J.H. Bonsel, R.H.B. Fey, H. Nijmeijer, Application of a dynamic vibration absorber to a piecewise linear beam system, *Nonlinear Dynamics* 37 (2004) 227–243.

[14] W. Fang, J.A. Wickert, Response of a periodically driven impact oscillator, *Journal of Sound and Vibration* 170 (1994) 397–409.

[15] O. Kopmaz, S. Telli, On the eigenfrequencies of a two-part beam-mass system, *Journal of Sound and Vibration* 252 (2002) 370–384.

[16] P.J. Holmes, The dynamics of repeated impacts with a sinusoidally vibrating table, *Journal of Sound and Vibration* 84 (1982) 173–189.

[17] N. Minorsky, *Nonlinear Oscillations*, Litton Educational Publishing Inc., New York, 1962.

[18] A.B. Nordmark, Non-periodic motion caused by grazing incidence in an impact oscillator, *Journal of Sound and Vibration* 145 (1991) 279–297.

[19] J. de Weger, W. van de Water, J. Molenaar, Grazing impact oscillations, *Physical Review E* 62 (2000) 2030–2041.